Available online at www.sciencedirect.com
SCIENCE DIRECT
Journal of Membrane Science 276 (2006) 208–220
journal of MEMBRANE SCIENCE
www.elsevier.com/locate/memsci

The capture and release of biomass in a high voidage fibrous microstructure: Mechanisms and shear stress levels

T.E. Bustnes*, C.F. Kaminski, M.R. Mackley

University of Cambridge, Department of Chemical Engineering, Pembroke Street, Cambridge CB2 3RA, UK

Received 23 June 2005; received in revised form 19 September 2005; accepted 21 September 2005
Available online 28 November 2005

Abstract

This paper is concerned with the capture and release of flowing biomass in high voidage fibre networks, and the work is relevant to a number of areas including filtration and biomass growth within scaffold structures. Experiments were carried out using a micro scale visualisation flow cell and a laboratory scale filter with similar hydrodynamic conditions and these apparatus were used to establish the dominant modes and mechanisms of deposition during steady flow, and also the efficacy of oscillatory fluid flow for the re-suspension of deposited biomass. Numerical simulation was used to elucidate the flow characteristics through a 'clean' fibre network. Quantitative image analysis of in situ confocal laser scanning microscope data from the flow cell was conducted, obtaining both the local void fraction and surface area exposed to flow as the filtration progressed. The laboratory scale filter apparatus gave the overall filtration efficiency and pressure difference data, and also provided model parameters to estimate the filter coefficient λ as a function of the deposit level in the filter. By combining these model parameters with the image analysis results, it was possible to obtain the deposit profile in the filter bed as the filtration progressed and also the average shear stress acting on the biomass deposit as a function of fluid drag. The experimental results showed that the high voidage fibre network was an effective way of capturing biomass, and that filter ripening, steady-state capture and breakthrough are all present during the course of a filter run. During biomass filtration, the average shear stress acting on the biomass started at approximately 1.0 Pa and gradually rose to a peak of 6.5 Pa, which was the maximum sustainable by the deposit. Thereafter, a reduction in the shear stress indicated rearrangement of the deposit to zones further downstream in the filter. Subsequent high intensity oscillatory fluid flow was partially effective at removing the biomass deposit both in the micro flow cell and the laboratory filter experiment, with shear stress levels during this high intensity oscillatory flow starting at approximately 65 Pa with a fully loaded fibre network, and decreasing to 7.5 Pa as the filter medium approached a 'clean' state.

Keywords: Filtration; Shear stress; Biomass; Attachment; Detachment; High voidage

1. Introduction

The filtration of particle suspensions through porous media is of interest in areas as diverse as pharmaceutical production [22], oil production from subsurface wells [16,33,37,19], ground water seepage [27,2,28] and purification of molten metals [1,38]. The principal objectives of these filtration operations are to remove particulates and/or to maximise filter runs by preventing clogging of the filter medium. One of the main research objectives has been to create or modify porous media (see, e.g. [21,35]) or particle suspensions (see, e.g. [7,23,30,34]) to maximise particle capture and the solids holding capacity without the development of high flow resistance in the filter. In order to accomplish this, it is important to establish the predominant mechanisms for particle capture for each system of particle suspension and porous media.

In deep-bed filtration of hydrosols, particle capture in idealised systems have previously been identified to be a consequence of Brownian motion, electrostatic interactions, interception, hydrophobic effects and gravity settling [31]. The predominance of these mechanisms over mechanical pore clogging by large particles assumes that the filter pore size is substantially larger than the suspension particles, which is generally how deep-bed filters are designed [25]. Model systems with various liquid phase properties (e.g. ionic strength, temperature) and spherical or essentially non-deformable particles have often been used both in experimental (see, e.g. [6,9,15,26]) and theoretical studies (see, e.g. [29,31]) on capture

* Corresponding author. Tel.: +47 47332466/+47 52713362; fax: +47 52700471.
E-mail address: bustnes@polytec.no (T.E. Bustnes).

0376-7388/$ – see front matter © 2005 Elsevier B.V. All rights reserved.
doi:10.1016/j.memsci.2005.09.054

within porous media. However, in biological systems, biomass aggregates are rarely rigid or spherical structures, and can be described as 'fractal' in nature [11]. For this class of particulate systems, where particles are highly deformable and have an appreciable internal permeability to flow [17,36], the dominant capture mechanisms and resulting deposit morphology may differ significantly from idealised cases.

On startup, most deep-bed filters initially show a gradual improvement in their ability to capture solids. This is known as filter ripening, and has been attributed to the initial capture of particles leading to an increased surface area of capture, together with an improvement in surface interactions [9]. This is followed by a steady-state period, and thereafter particle breakthrough, which is characterised by a rise in the effluent solids concentration [20]. The precise mechanisms for these observations are dependent on the fluid-particle-medium system and the prevailing hydrodynamic conditions. In the practical operation of filter systems, pressure difference measurements are commonly used to stop filter runs before the onset of breakthrough [18], but it has been suggested that for some filtration systems, wall shear stress measurements show better correlation with filter performance [10].

In our research, we have established that various high void fraction fibre materials are generally better than granular or foam media at capturing biomass from domestic wastewater [4]. This means that the detailed internal geometry of the filter medium is important in biomass particle capture. We have also explored the use of oscillatory fluid flow for the detachment and re-suspension of these biomass aggregates. We have briefly reported on visualisation studies relating to biomass capture in high voidage fibrous filters [5] and also described aspects relating to the hydraulic response of the system [3]. In this paper, particle capture mechanisms are identified and by using confocal laser scanning microscopy (CLSM), void fractions and surface areas are determined within the high porosity filter. From matching laboratory scale hydraulic experiments, it was then possible to establish shear stress values where capture can occur and also estimate the maximum shear stress that captured biomass can sustain before detachment occurs. Intense fluid oscillation is shown to be partially effective in removing biomass from a loaded filter and again, shear stress values are estimated for this part of the cleaning process.

2. Theoretical background

The normal approach in the mathematical description of deep-bed filtration is to conduct a mass balance across a filter section [32,31]:

$$u\left(\frac{\partial c}{\partial z}\right)_{\theta}+\left(\frac{\partial \sigma}{\partial \theta}\right)_{z}=0 \tag{1}$$

where c is the suspension concentration at depth z from the filter inlet, θ a 'corrected time' variable and σ is the specific deposit of the filter bed.

The concentration of suspension is related to the depth into the filter using a parametric rate equation, usually of the form

$$-\left(\frac{\partial c}{\partial z}\right)_{t}=\lambda c \tag{2}$$

where t is time and λ is the filter coefficient, and depends on the filter medium, the fluid suspension and the state of deposition of the filter medium. The difference between the time variable t and 'corrected time' variable θ is the interstitial time of travel of a fluid element between the filter entry and depth z, and this difference is in most practical cases negligible [32].

One important implication of an analysis where the rate equation is first order in c is that the gradient of deposit with depth is constant at a given level of deposit σ [12]. This implies that the specific deposit curves through the filter are interchangeable by translation [32], and that a 'deposit front' should exist that travels with a constant velocity through the filter. The 'deposit front' velocity is given by

$$V_{\mathrm{F}}=\left(\frac{\partial z}{\partial \theta}\right)_{\sigma}=\frac{(\partial\sigma/\partial\theta)_{z}}{(\partial\sigma/\partial z)_{\theta}}=\frac{(\partial\sigma/\partial\theta)_{z}}{\lambda\sigma}. \tag{3}$$

This theoretical framework allows a deposit profile and in a filter section to be estimated, provided the specific deposit is known with time at a particular depth in the filter section.

3. Micro flow cell visualisation

3.1. Experimental set-up

In order to directly view the deposition and release of biomass in a polyester fibre section, a flow cell was constructed as shown in Fig. 1. The flow cell consisted of a poly(methyl methacrylate) block of dimensions 60 mm × 24 mm × 10 mm with a channel of dimensions 35 mm × 5 mm × 1 mm milled into its base. A known mass of heat bonded polyester fibres (Algarde fish pond filter material) was placed in the channel to give an average void fraction of 0.95. Entry and exit holes were drilled through the block, and a glass cover slide was held in place at the base of the block with double-sided sellotape to close the flow channel. The feed consisted of domestic wastewater which had passed through primary treatment and trickling filter secondary biological treatment before being collected at the Milton Sewage Works (AWG, Cambridge, UK).

Two syringe pumps and one miniature electro-mechanical fluid oscillator were connected to the feed line. One of the sy-

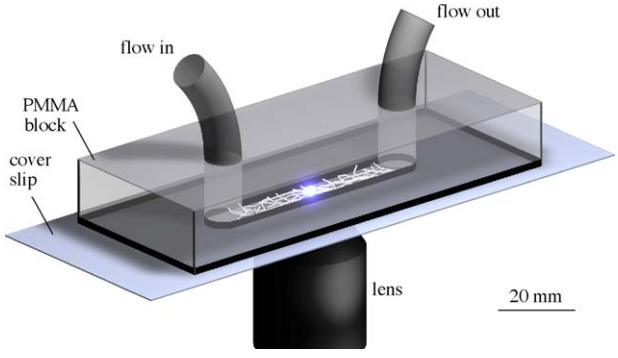

Fig. 1. Micro flow cell consisting of a poly(methyl methacrylate) (PMMA) block with entry and exit holes and a channel milled at its base. Polyester fibres at a bulk void fraction of 0.95 were placed in the channel and a glass cover slip was attached to the bottom of the PMMA block using double-sided sellotape.

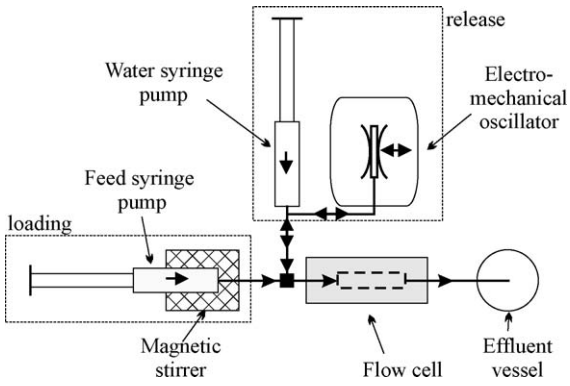

Fig. 2. Experimental set-up for visualisation using LSCM. The dashed rectangles indicate the equipment used for the loading and release of biomass from the fibre matrix in the flow cell.

ringe pumps was used to introduce biomass suspension into the flow cell. In order to keep the particles from sedimenting in the biomass feed syringe, it was necessary to place a small magnetic stirrer bar inside the syringe. The other syringe pump and the fluid oscillator were used for regeneration of the flow cell once the fibre matrix was fully loaded with biomass. This was accomplished by a combination of oscillatory fluid flow (to re-suspend the biomass) and superimposed net flow (to transport the re-suspended biomass away). Both filtrate and re-suspended biomass after filter regeneration were transported through the effluent line to a common receptacle. An overview of the experimental set-up is seen in Fig. 2.

The micro flow cell was placed on an Olympus IX50 inverted CLSM equipped with a 488 nm (Ar) laser line. Initially, the flow cell was filled with tap water and image sections of 1408 μm × 1408 μm size were recorded at 7.5 μm depth intervals for the first 500 μm from the inside surface of the microscope slide (c.f. Fig. 1). Such three-dimensional image stacks were recorded using (1) reflected light and (2) fluorescence of the bioaggregates from the flow cell. The scanned image stacks were located 17 mm from the filter inlet and in the middle of the flow channel. The reflected and fluorescent wavelengths were directed to different photomultiplier tubes (PM channels) and recorded separately. It was found that the polyester fibres did not exhibit intrinsic fluorescence and they were therefore captured in the reflection PM channel. When biomass particles were introduced into the flow cell, it was discovered that they showed sharp autofluorescence above 660 nm, and appropriate optical barrier filters were used to direct this wavelength to the other fluorescence channel.

Capture experiments were conducted at various superficial flow rates and a biomass concentration of 120 mg l^{-1}. The total duration of the capture experiment was 1 h. The net throughflow was stopped at regular intervals and a full three-dimensional image stack was recorded. In this way, the internal morphology of the biomass deposit within the flow cell could be followed with time.

After the filter section was saturated with biomass, the net throughflow was stopped. The miniature oscillator was started, delivering fluid pulsing to the flow cell and in this way dislodging and re-suspending deposited material. At the same time, the syringe pump with tap water was set to deliver a net superficial flow in order to transport the re-suspended biomass away from the flow channel. Regeneration continued in this way for 10 min. At regular intervals, the oscillatory flow was stopped and image stacks recorded.

In addition to obtaining three-dimensional images of the fibre and biomass deposit morphology within the flow cell, detailed numerical analysis of the image stacks obtained was used to give the internal specific deposit (σ) and the internal surface area exposed to flow (S) at any given time. This was accomplished with a purpose-written computer code using IDL software language.

3.2. Capture mechanisms

Fig. 3 shows superimposed fluorescence and reflectance images taken during filtration and regeneration. For these experiments, the superficial fluid flowrate was set to 4.4 mm s^{-1} for the capture. During regeneration, near-sinusoidal oscillatory conditions were set to 4.5 Hz and centre-to-peak amplitude of 11 mm, giving a peak superficial fluid flow of 320 mm s^{-1}. At the beginning of the capture experiment, some small particle aggregates attach directly to the fibres, probably with capture mechanisms similar to those reported in Tien [31]. However, most of the particle aggregates are seen to attach predominantly at fibre intersections (b). This enhances the capture at these sites, creating larger particle aggregates (c) and eventually an almost continuous network of particles (d). This explains the phenomenon of 'filter ripening', or the improvement of filtration efficiency with time, that has been documented in the literature (see, e.g. [9]). It also explains why the intersecting fibre geometry gives significantly better capture than polymer foams with similar void fractions [4].

In (d), obstruction of the laser light in parts of the image highlight the differences in biomass particle density and thus indicates the development of flow channels for these high biomass loadings. The flow channels will have progressively higher interstitial velocities as they constrict with time, and this means that particle break-off and/or non-attachment are the likely causes for particle breakthrough into the effluent. In the images presented, the morphology of the biomass deposit clearly changes with time. Additionally, a previous visualisation study [5], showed that small particles are re-entrained into the fluid flow. These two findings indicate that at least some of the particles that eventually break through to the effluent have been captured and subsequently sheared off.

After fluid oscillations, most of the attached biomass particles are removed and transported away (e). This oscillation intensity is clearly able to re-suspend most of the deposit in a relatively short time, and prolonging the oscillation time also reduces the amount of deposit left in the fibre matrix (f).

3.3. Void fraction and surface area determination using image analysis

Image analysis programming routines were developed using IDL programming language for void fraction and surface area calculations from the three-dimensional image stacks (see, Ref.

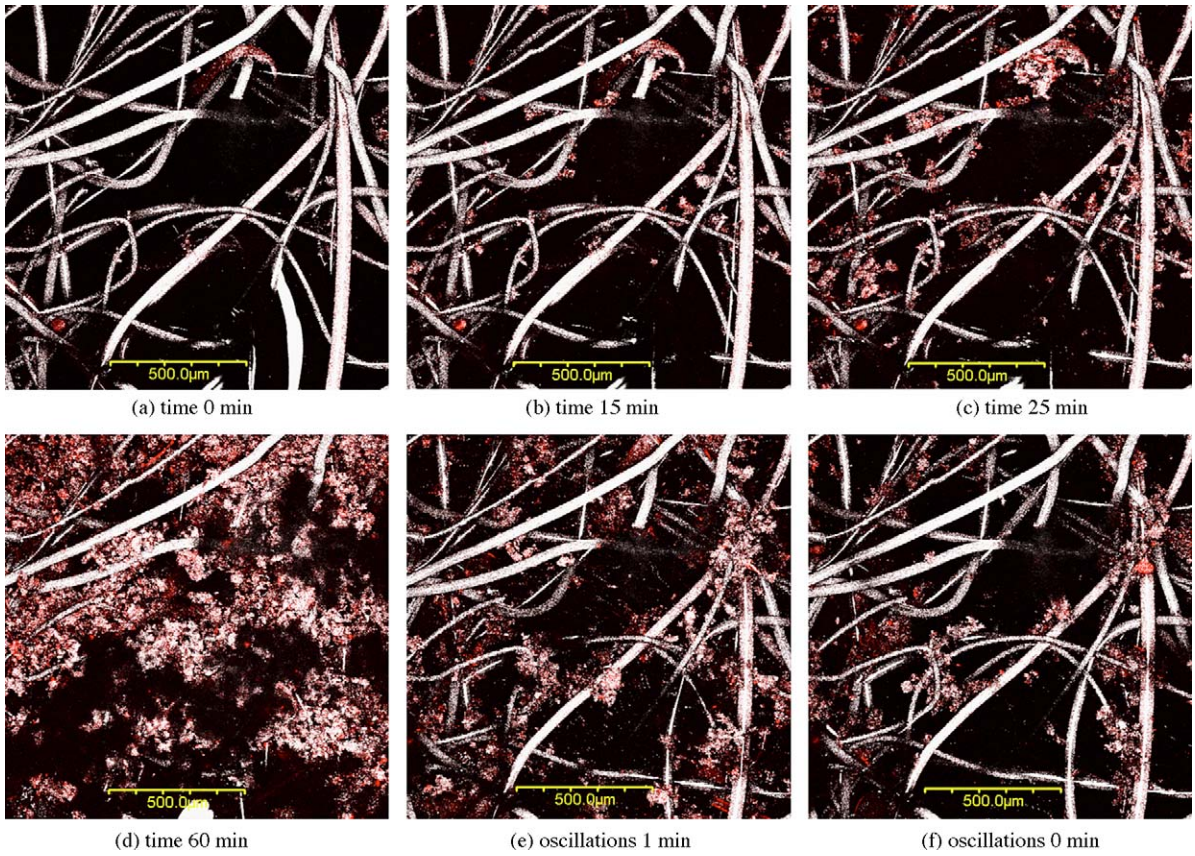

Fig. 3. LSCM experiment showing (a–d) capture and (e–f) release of biomass. The flow direction was from left to right at a superficial flowrate of 4.4 mm s^{-1} during biomass capture. The oscillations (left–right) were at a frequency $f = 4.5$ Hz and channel amplitude $a_{c\text{-}p} = 11$ mm, with a (left to right) superimposed net flow of water at 2.2 mm s^{-1} . Feed biomass concentration was 120 mg l^{-1}. Time (a) 0 min, (b) 15 min, (c) 25 min, (d) 60 min; oscillations (e) 1 min, (f) 10 min.

[4]). Prior to further analysis, the pixel intensities of each slice in the image stack were normalised to account for the reduction in reflectance and fluorescence intensity with depth into the filter. The porosity analysis consisted of 'thresholding' each image slice to distinguish voxels (three-dimensional pixels) representing voids from those representing fibres (reflectance channel) or biomass deposit (fluorescence channel). For the fluorescence channel, the 'solid' voxels were then summed and divided by the total number of voxels in the image stack to give the specific biomass deposit σ. For the surface area analysis, each fibre or biomass voxel was compared with its nearest neighbour in space to determine which surfaces were exposed to 'void' voxels. The exposed areas were then calculated and summed, and finally divided by the image stack volume to give the specific surface area S (Table 1).

Table 1
Porosities and specific surface areas (by image analysis) during capture and release of biomass

Capture time (min)	Porosity, ϕ	Specific surface area, S (m^{-1})
(a) 0	0.950	5200
(b) 15	0.946	5800
(c) 25	0.939	6400
(d) 60	0.857	18800
(e) 1 min (osc)	0.924	9200
(f) 10 min (osc)	0.935	7300

The biomass solids fraction is seen as a function of time for the recording position 17 mm from the entry to the flow cell in Fig. 4. The deposit initially builds up in an exponential fashion, but after about 35 min a plateau is reached and the maximum loading possible for this section of view is obtained. After the filtration is stopped at 60 min, the fluid oscillations progressively bring the biomass levels down to near the starting value.

Fig. 5 shows the relationship between the internal surface area exposed to flow S and the biomass solids loading σ. This linear relationship may be used to estimate the internal surface area exposed to flow for a filter section for which the overall deposit is known, and this result is used in a later section.

In the sections below, the image analysis results are compared with values obtained using a laboratory scale filter unit. In addition, the results of the filtration study are used to expand the flow cell results by providing model parameters and pressure difference data for this filtration process.

4. Laboratory filtration experiments

The laboratory scale experiments used a 54 mm diameter and variable depth cylindrical filter of the adjustable void fraction. 'Clean' filter experiments were conducted with different filter porosities and flowrates, but the main biomass filtration experiments were carried out with a 32 mm depth filter of initial porosity 0.95. The superficial flowrates and feed concentrations used

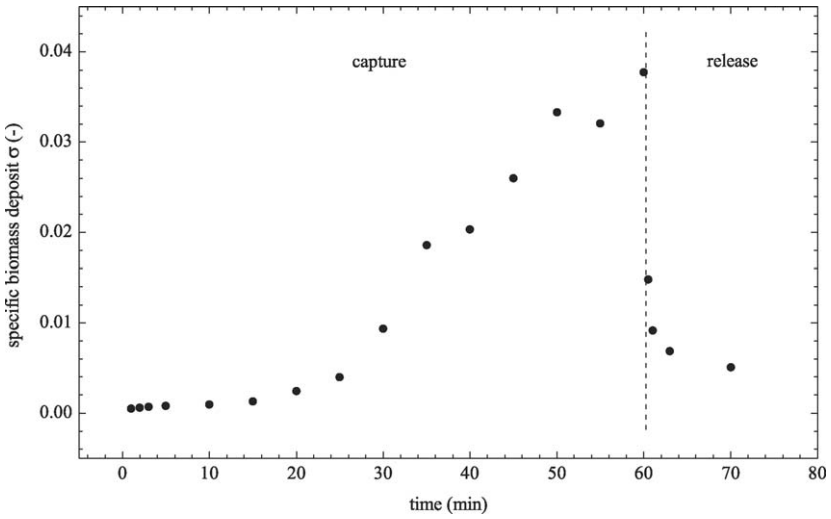

Fig. 4. Results from specific deposit determination using image analysis with IDL software.

for these experiments were the same as for the micro flow cell. By analysing the suspended solids concentration of the feed and effluent of the filter, the biomass accumulation in the filter could be calculated from a mass balance. More extensive results using this laboratory scale filter are reported in Bustnes and Mackley [3].

4.1. Experimental set-up

A filter rig was constructed according to Fig. 6, incorporating magnetically stirred feed tanks, a feedback-controlled peristaltic pump (in order to ensure constant flowrate), filter section and turbidity measurement unit. Below the filter section, a hydraulic piston was installed in order to oscillate the fluid in the filter column and thereby provide sufficient hydrodynamic drag on deposited particles to re-suspend them and hence regenerate the filter.

The operation of the filter when filtering biomass feed consisted of pumping the particle suspension through a polyester fibre section of void fraction 0.945 and depth 32 mm. During filtration, the differential pressure across the filter column was measured using pressure transducers. Also, feed and, at regular intervals, effluent samples were taken and analysed off-line for suspended solids according to Clesceri et al. [8].

4.2. Filtration results

In Fig. 7, the pressure response of the 'clean' polyester fibre filter is plotted for various void fractions and flowrates. The hydrodynamic pressure difference is clearly a linear function of the flowrate, and decreases with the void fraction. Fig. 8 shows the oscillatory flow pressure response of the filter, for a centre-to-peak amplitude of 20 mm and frequency 0.5 Hz. The measurements show that the pressure response closely follows the

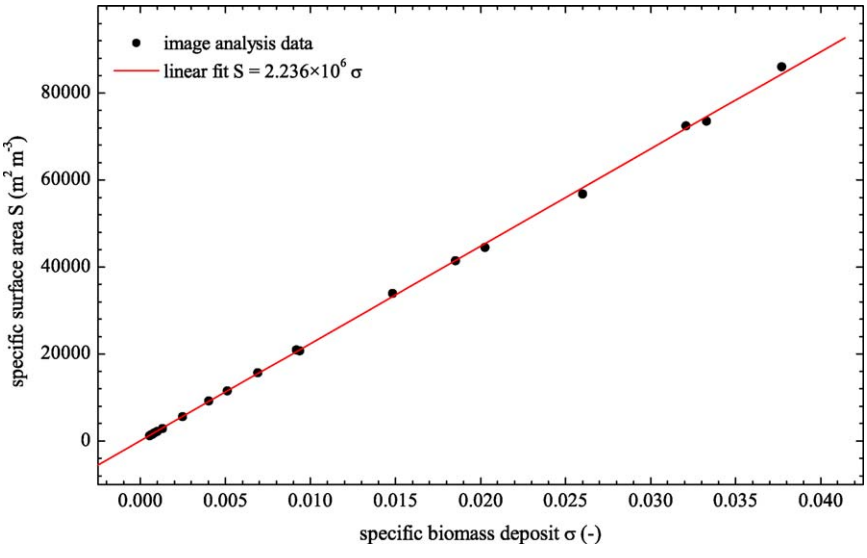

Fig. 5. Relationship between internal surface area exposed to flow and specific biomass deposit. In this figure, the solids fraction and surface area contributions from the fibres are omitted.

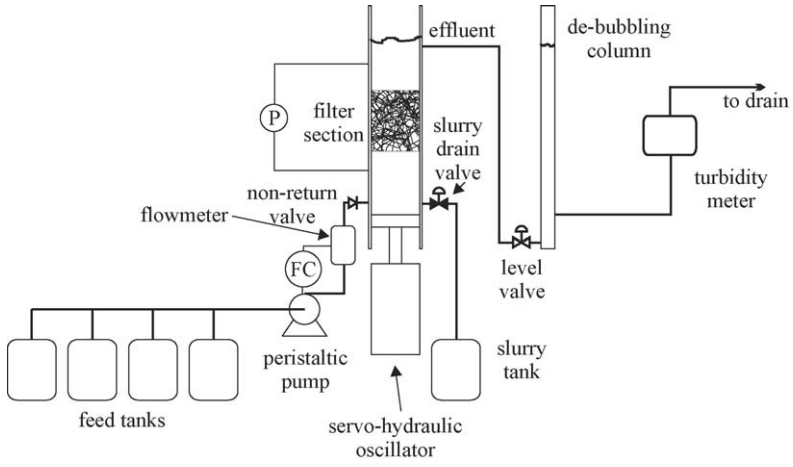

Fig. 6. Schematic showing the main components of the biomass filtration unit. Feed is pumped from the feed tanks using a peristaltic pump and enters the base of the filter column after passing a flowmeter, which is used for feedback control of the pump. Filtrate exits at the top of the filter column and passes through a de-bubbling unit and subsequently a turbidity measurement device. The piston under the filter section can oscillate the fluid in the filter on filter clogging, and the slurry thus formed is drained through the side valve at the base of the column. The pressure difference across the filter is also measured using two pressure sensors.

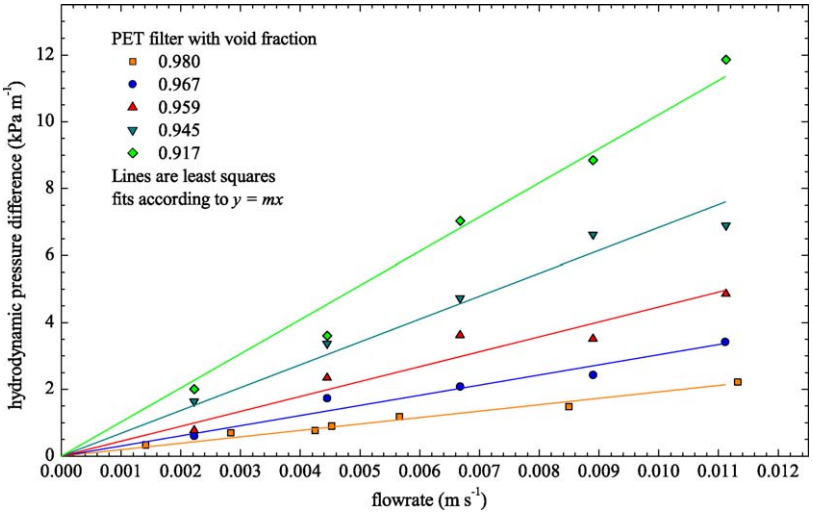

Fig. 7. Pressure difference across filter section for various void fractions and flowrates.

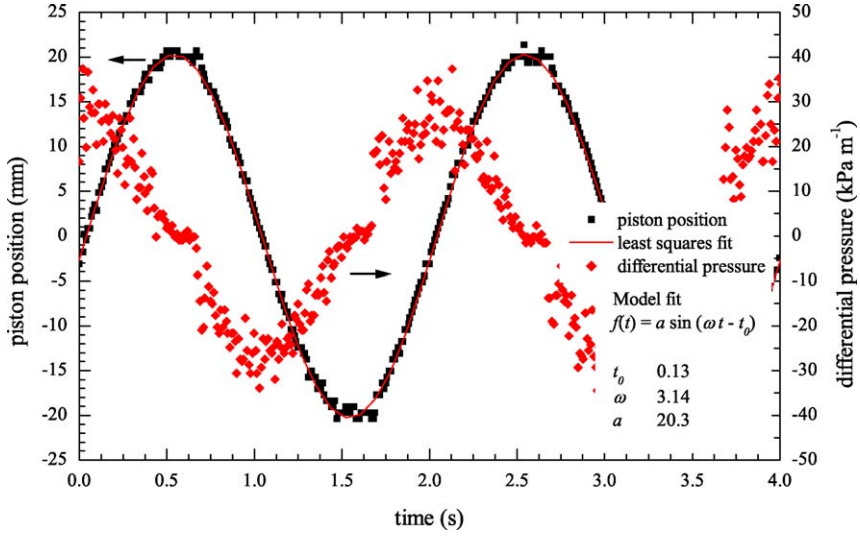

Fig. 8. Oscillatory flow response of filter of void fraction 0.95 at frequency $f = 0.5$ Hz and amplitude $a_{c\text{-}p} = 20$ mm.

piston velocity without a significant phase lag between the fluid flow and the pressure difference.

The shear stress at the fibre walls as deposition takes place is more fundamental than pressure difference information alone in terms of events such as ripening, steady state and particle breakthrough. For a fluid flowing with laminar flow through a porous section of constant cross-section and depth l, the average shear stress at the porous medium surface, τ_w, may be calculated by an overall force balance to give:

$$\tau_w = \frac{\Delta P}{l}\frac{1}{S} \tag{4}$$

where S is the specific surface area of the medium. Using the expression for S for a fibrous medium given in Appendix A, Eq. (4) may be written as:

$$\tau_w = \frac{\Delta P}{l}\frac{d_f}{4(1-\phi)} \tag{5}$$

For a filter medium of porosity $\phi = 0.945$, Fig. 7 shows that a superficial flowrate of 4.4 mm s^{-1} through a clean filter section produces a pressure difference of 3 kPa m^{-1}, giving an average shear stress of 0.53 Pa. This is the order of magnitude of shear stress acting on the first deposit that attaches to the fibre network. The wall shear stress for a 'clean' filter section can in this way be computed from knowledge of the fibre diameter and pressure difference measurements alone. During deposition, however, the internal surface area exposed to flow is dependent on the precise deposit morphology within the filter section, and is therefore not possible a priori to determine the local shear stress within the filter bed.

Typically, a filtration run using biomass feed suspension yielded information about the filter effluent turbidity and solids content, and the pressure difference across the filter. The 32 mm filter gave the results shown in Fig. 9. The feed concentration was determined to be 123 mg l^{-1}, very similar to the feed for the micro flow cell. In terms of effluent solids concentration, the figure shows that the initial rise to just under 10 mg l^{-1} is followed by a *drop* in the effluent concentration to about 5–7 mg l^{-1} indicating *filter ripening*. A relatively steady solids concentration is thereafter observed until 30 min of filtration. Subsequently, a sharp rise is evident, indicating a *breakthrough* of biomass to the effluent.

The hydrodynamic pressure difference across the filter (Fig. 9) shows a sharp rise in the flow resistance after the initial ripening period, with a lower gradient as the fibre network gradually fills. The inflection points on the pressure curve indicate a possible re-arrangement of biomass within the filter and the development of flow channels, as confirmed by the micro flow cell results described in the previous section. Breakthrough takes place immediately after a flow perturbation (seen at about 32 min in Fig. 9), accompanied by a perturbation in the pressure difference and also a peak in the effluent turbidity. However, the subsequent gradual rise in the effluent solids concentration and turbidity indicates that breakthrough was in any case imminent when the flow perturbation took place. It is significant, however, that perturbation in the flow has such a large effect on the ability of the filter to capture particles, since oscillatory fluid flow at a significantly higher intensity then these flow perturbations was used for regeneration of the filter section.

In the next section, the 'clean' filter pressure difference values obtained from the laboratory scale filter are compared with simulation results obtained using Fluent simulation software.

5. Numerical flow simulation

5.1. Geometry, mesh generation and boundary conditions

Three different three-dimensional geometries and meshes similar to that shown in Fig 10 were generated, representing fibres of diameters in the range 20–40 μm oriented transverse to the flow. The number of fibres was adjusted to give approximately equal volume fraction contributions from the three diameters for a final void fraction close to 0.95 in the simulation cube, which had sides of length 400 μm . The only variation between the geometries were the different spatial positions of the fibres within the simulation cube. Fibres were placed at random locations within the simulation cube, with some restrictions placed

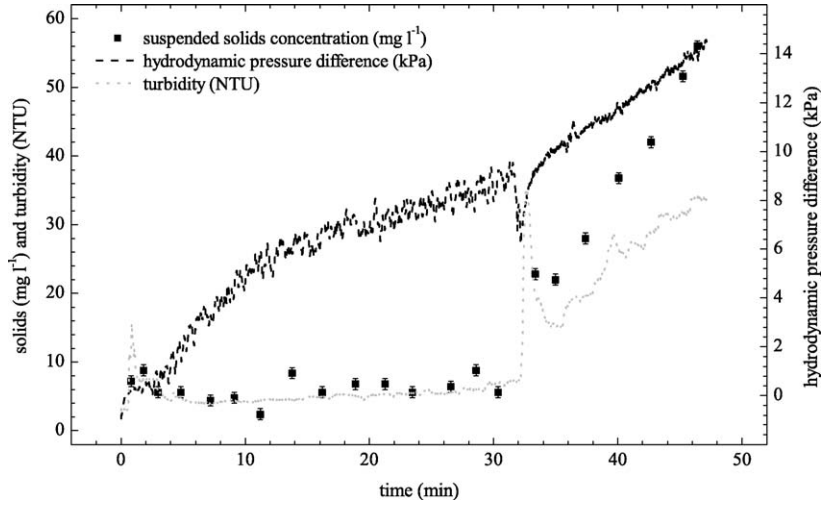

Fig. 9. Data obtained from 32 mm depth laboratory scale filter using biomass feed of concentration 123 mg l^{-1}. The event at 30 min is due to a flowrate perturbation.

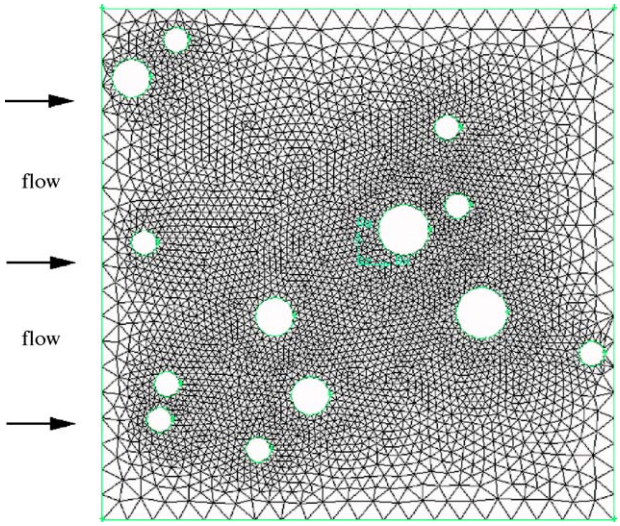

Fig. 10. Example of simulation mesh as created by Gambit mesh generation software. The mesh is a three-dimensional mesh where all the sections in the z-direction are the same, and only a two-dimensional slice at $z = 0$ is shown here.

on their relative position: fibres could not overlap each other or touch the boundaries of the simulation cube, as this created difficult boundary conditions.

Meshing was accomplished by pre-setting the number of nodes on the fibre surfaces to 15, 20 and 30 (fine mesh) for the three respective fibre diameters and on the edges of the simulation cube to 20 (coarse mesh) so as to give accurate meshing where required while minimising the number of mesh cells. The results presented in this paper were obtained using an unstructured triangular meshing scheme with a total of approximately 146,000 mesh cells. The dependence of the results on mesh size was tested and it was found that a mesh containing 407,000 mesh cells gave results deviating from those reported by less than 5%.

For the three mesh geometries, periodic boundary conditions were imposed on the inflow (left hand side) and outflow (right hand side) faces. This enabled simulation of steady-state flow. In addition, the remaining four faces of the simulation cube were made into symmetry planes. This made the simulation close to one of fully developed steady-state flow, with the exception that no flow was allowed across the symmetry planes. Mathematically,

$$\frac{\partial u_x}{\partial y} = 0, \quad \text{at } y = \{-200, 200\} \quad \text{and} \quad \frac{\partial u_x}{\partial z} = 0,$$

$$\text{at } z = \{-200, 200\}$$

where the positive x-direction is the bulk flow direction.

Initial velocity conditions in all simulation cells were set to the superficial velocity in the x-direction, and a solution was obtained using the implicit, numerical solver routine in Fluent. Computational iterations were carried out until the sum of the errors for each of the velocity components and the continuity equation were all below the tolerance threshold, set at 10^{-3}.

5.2. Simulation results

For various superficial flowrates, the hydrodynamic pressure differences are plotted in Fig. 11, together with selected experimental results from the previous section. There is a significant variation between the different geometries, and this must be expected as flow channelling would be present to a greater or lesser extent depending on the fibre geometry. Even though the variation is large, the order of magnitude of the pressure differences corresponds well with the experimental results from the laboratory scale filter.

The velocity vector map corresponding to the simulation mesh given in Fig. 10 is shown in Fig. 12. The velocity map shows a large difference in the velocity magnitudes for different spatial locations. The largest velocity recorded is almost three times the superficial velocity, and it is therefore probable that preferred locations for deposition exist in this geometry.

Simulations also give the possibility of estimating the wall shear stresses at the fibre surface. The shear stress results were

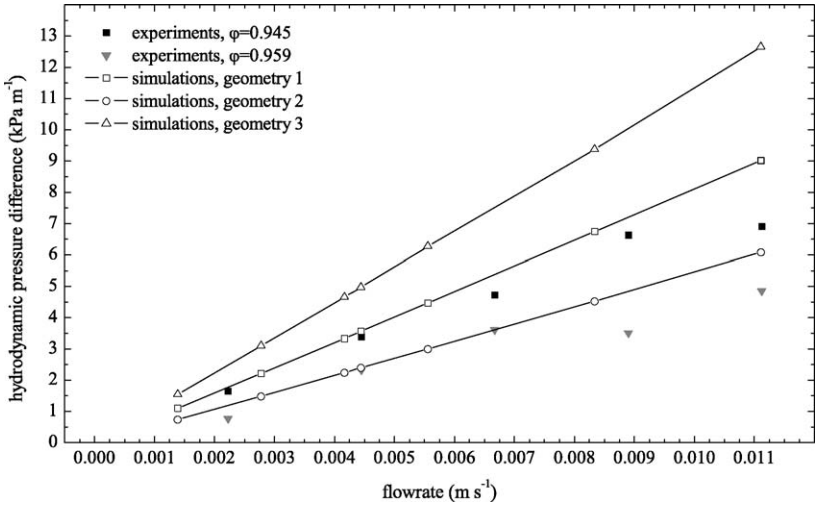

Fig. 11. Hydrodynamic pressure difference from simulations of fully developed flow in different geometries. The simulation geometries consisted of 'fibres' of diameter 20, 30 and 40 μm placed at random locations transverse to the flow.

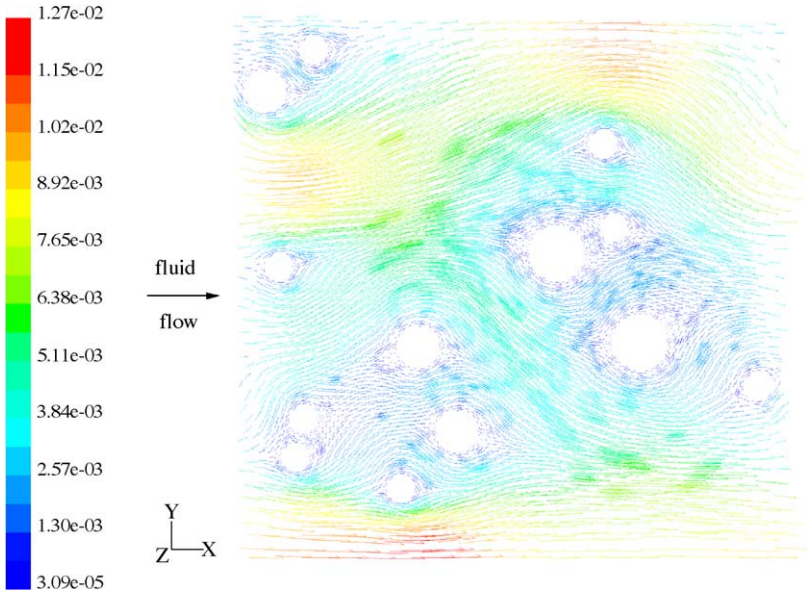

Fig. 12. Velocity vector map obtained from numerical simulations of flow through fibre section with void fraction 0.955 at superficial flowrate of 4.4×10^{-3} m s^{-1}. Colours indicate velocity magnitude. (For interpretation of the references to colour in this figure legend, the reader is referred to the web version of the article.)

in the range 0.01–1.25 Pa depending on the position on the fibre surface, with an average shear stress for all the three simulation geometries of 0.36 Pa. This agrees well with the experimentally obtained values in the previous section.

6. Filter behaviour during biomass deposition and release

In order to assess whether the filter behaviour at the flow cell and laboratory filter scales are comparable, it is instructive to compare the development of the average deposit levels in the two experimental filter set-ups as time progresses. This is complicated in the micro flow cell because the spatial deposit profile from the filter inlet is not known, making the average deposit level in the filter inaccessible.

If the specific deposit is determined as a function of time t at a particular depth z in the filter, Eq. (3) can be used to infer the specific deposit profile with filter depth. In effect, this involves using $(\partial\sigma/\partial t)$ values from the micro flow cell and values for λ estimated from laboratory scale experiments to assess the 'deposit front' migration from the flow cell inlet. For each level of deposit recorded by image analysis, the 'front velocity' was calculated (Fig. 13), and with a zero-level initial deposit in the filter, the resulting time development may be plotted as in Fig. 14. The area under each of these curves can be determined numerically and hence an average biomass deposit and filter void fraction found as a function of time.

It is interesting to note that the prediction of Herzig et al. [12] that the 'front velocity' at all deposit levels should remain constant with time is not valid. This discrepancy between theoreti-

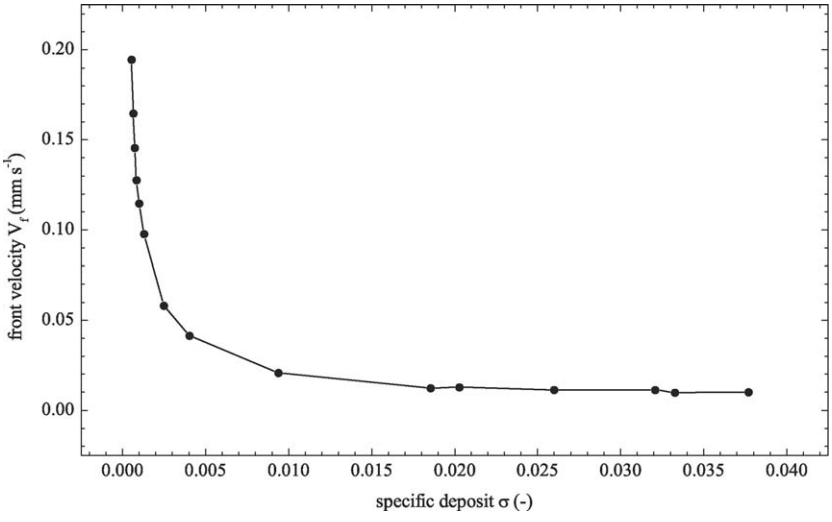

Fig. 13. Deposit 'front velocity' as obtained from Eq. (3) taken from Herzig et al. [12].

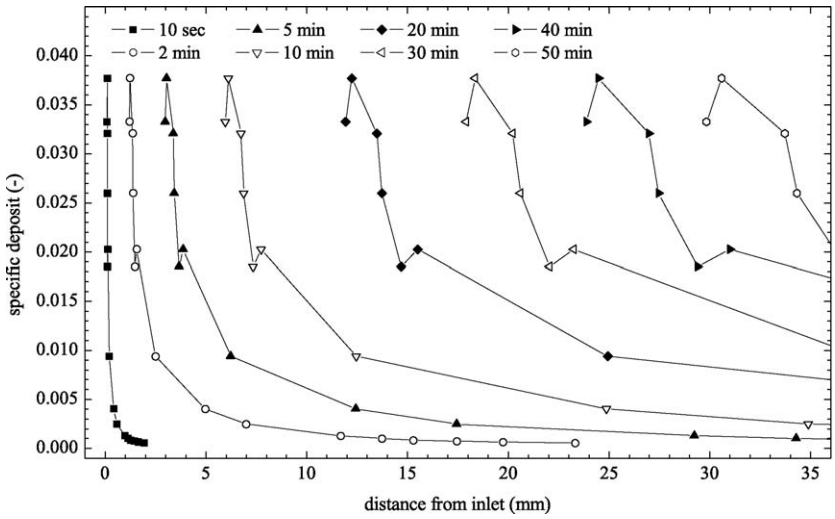

Fig. 14. Deposit profiles in micro flow cell at different filtration times.

cal predictions and experiment was also mentioned in Tien and Payatakes [32], but no experimental data to this effect were presented. The result of the progressive reduction in the 'front velocity' is that the deposit profile flattens as it progresses through the filter, i.e. low levels of biomass reach the exit to the filter within the first 5 min while the 'heavy' deposit progresses at the much slower rate of about 10 $\mu m\,s^{-1}$.

Fig. 15 shows the comparison of experimental void fractions ϕ as obtained from the flow cell and laboratory filtration experiments, the latter given by

$$\phi = \phi_0 - \frac{\sigma_L}{\rho_{bm}} \tag{6}$$

where ϕ_0 is the starting void fraction (0.95), σ_L is mass-based specific deposit (in $g\,m^{-3}$) and ρ_{BM} is the biomass density, as before. The average void fraction profiles with time are remarkably similar for the two experimental methods, given the differences in geometry and the very different methods for their estimation.

Given the pressure difference data in Fig. 9, the void fraction development for the laboratory scale filter given in Fig. 15 and the relationship between the deposit level and the internal surface area exposed to flow given in Fig. 5, Eq. (4) may be used to estimate the average shear stress levels acting on the biomass deposit *during* deposition. A plot of τ versus t is shown in Fig. 16. The figure shows a progressive build-up of average wall shear stress from initially about 1 Pa (a level somewhat above the 'clean' filter values determined by experiment and simulation) to about 6.5 Pa at a time of 12 min. The shear stress thereafter drops until it reaches a local minimum at around 30 min, at which time biomass breakthrough was originally observed (Fig. 9).

It is clear from Fig. 16 that the shear stress levels build-up until the drag forces on the deposited biomass become unsustainable. This observation is consistent with a model in which the peak of the shear stress curve signifies the point at which biomass from the highest levels of deposit are broken off and re-captured downstream. This rearrangement of biomass deposit

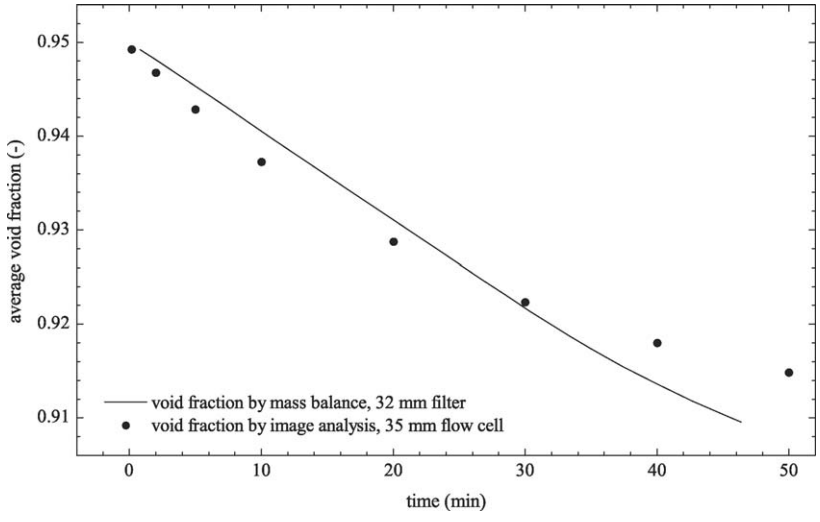

Fig. 15. Average void fraction in laboratory scale filter compared with that of the micro flow cell.

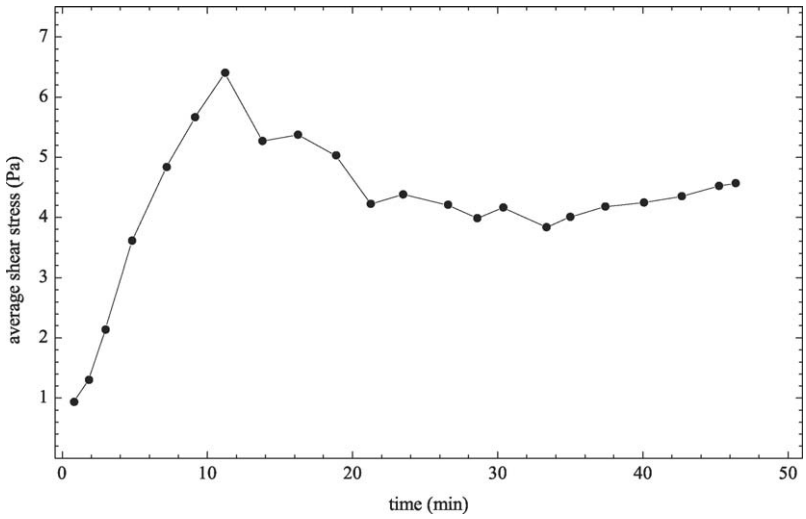

Fig. 16. Wall shear stress with time as determined by Eq. (4) and data provided from laboratory scale and flow cell experiments.

to zones deeper into the filter takes place until the flow cell is saturated and significant biomass finally escapes to the effluent (30 min).

During oscillatory flow, crude estimates of the shear stress may also be obtained from the data presented. By observing that the peak pressure follows the peak velocity (Fig. 8), it is possible to linearly extrapolate the recorded pressure difference from the end of the deposition experiment ($\Delta P/l \sim 0.47\,\mathrm{MPa\,m^{-1}}$) to the peak flow velocity at the beginning of regeneration (giving $\Delta P/l \sim 6.73\,\mathrm{MPa\,m^{-1}}$). From Eq. (4), this gives an estimated peak oscillatory shear stress at the initial phases of regeneration of order 65 Pa. Together with the periodic flow reversal, this is sufficient to remove most of the deposited biomass as seen in Fig. 3 and reported in Bustnes and Mackley [3] from laboratory scale experiments.

It is also possible to use the steady and oscillatory flow data in Figs. 7 and 8 with Eq. (5) to estimate the maximum shear stresses on the biomass deposit as the fibre bed approaches the 'clean' state towards the end of oscillatory flow regeneration. From the steady flow pressure difference at $4.4\,\mathrm{mm\,s^{-1}}$ ($\Delta P/l \sim 3\,\mathrm{kPa\,m^{-1}}$), the average shear stress is approximately 0.53 Pa. Using the maximum oscillatory pressure difference recorded during oscillatory flow ($\Delta P/l \sim 40\,\mathrm{kPa\,m^{-1}}$), the average shear stress at the fibre surface at these oscillatory conditions would be of order 7.6 Pa. This just above the maximum level during deposition, and therefore provides an insight into why it is that not all the biomass is removed by the oscillatory flow motion.

7. Conclusions

In this paper, results are presented for the micro scale visualisation of steady flow capture and oscillatory flow release of biomass from a high porosity polyester fibre network. Three-dimensional reflectance and fluorescence image stacks were recorded at regular intervals during capture and release using a CLSM. The images show that the predominant mode of capture was for large biomass aggregates to become intercepted at fibre crossing points, and for smaller aggregates to subsequently adhere to these captured particles. Eventually, as the fibre network filled with biomass, flow channels formed and no further net capture took place. Intense oscillatory fluid flow was able to re-suspend most of the biomass deposit, which was transported away by a net flow of water.

Quantitative image analysis was carried out on the image stacks, yielding information about the local specific deposit and surface area exposed to flow in the section covered by the image stack. The local deposit level initially rose in an exponential fashion, and then plateaued at a deposit level of approximately 4% . The relationship between the specific deposit and the internal surface area exposed to flow was also established as linear.

Laboratory scale filter experiments were conducted with a cylindrical filter of diameter 54 mm and variable filter depth and void fraction. For the steady flow of water through a 'clean' filter, analysis of the pressure difference results showed that the wall shear stress on the fibre surface was approximately 0.53 Pa for a steady flow of $4.44 \times 10^{-3}\,\mathrm{m\,s^{-1}}$ through a filter of void fraction 0.945. Numerical flow simulations gave results in the range 0.01–1.25 Pa depending on the position around the fibre circumference, with an average of 0.35 Pa over all angles. The experimental and simulation results are thus of the same order of magnitude.

When using biomass feed to the laboratory scale filter, the filter went through different phases including filter ripening, where biomass filtrate concentration decreased with time. Then, a steady-state phase was reached, followed by breakthrough of biomass to the effluent. Feed and effluent concentration data were used to establish model parameters to determine the filter coefficient as the filtration progressed. Using this information, a deposit 'front velocity' was determined for the micro flow cell and hence the deposit profile and average void fraction with time were established. The void fraction results from the flow cell were compared with the laboratory scale filter found by a mass balance, and in this way it was shown that using the CLSM

and image analysis can relatively accurately determine the state of deposition of biomass in such a filter system.

The relationship between the specific deposit and internal surface area exposed to flow was used to estimate the shear stress levels in the laboratory scale filter unit with time. This gave the insight that shear stress levels build-up to a maximum of about 6.5 Pa, at which point the shear forces probably break off some biomass deposit and move it to other deposition sites further downstream in the filter. Upstream flow channels are therefore created, as observed qualitatively from the CLSM data. When deposit rearrangement finally renders the filter saturated with biomass, particle breakthrough is observed. Extrapolation of these results was also used to estimate the shear stresses during oscillatory flow release, and it was found that the average shear stress in the section started at approximately 65 Pa and diminished to about 7.5 Pa as the filter approached its previously 'clean' state. This level of shear stress is comparable to the maximum sustainable by the biomass during steady flow, and explains why oscillatory flow of this intensity is not able to remove all the deposited matter from the filter.

Data in this paper provide information for future work where flowing biomass is involved within confined volumes. In particular, a shear stress value of about 6.5 Pa represents a critical value. Below this stress level, biomass capture onto a filter medium and onto captured biomass itself can occur. Above this level, further deposition of biomass will not occur and removal of clumps of biomass from attached deposits becomes possible. Clearly, the exact value of this critical shear stress will depend on the nature of the biomass and surfaces under consideration.

In the micro flow cell image analysis, the deposit solids fraction was found to be directly proportional to its associated surface area exposed to flow during biomass deposition. In this particular case, therefore, the average interstitial velocity scales linearly with the surface shear stress levels. This implies that the critical shear stress identified in this paper is related to the critical interstitial velocity in the filter medium. The latter is far easier to assess experimentally by calculating the filter void fraction (e.g. by a mass balance) as the deposition occurs. However, the relationship between the deposit solids fraction and surface area exposed to flow is crucially dependent on the degree of packing of the deposit and is in general not necessarily a linear function during filtration. The shear stress at the filter medium surface is therefore the more fundamental quantity for assessing the critical condition where no more deposition occurs in a filter.

Acknowledgements

The authors wish to thank the Engineering and Physical Sciences Research Council (UK) for an 18-month grant under the WITE initiative, and Trond E. Bustnes wishes to thank the State Educational Loan Fund (Norway) for their financial support. The authors also wish to thank AWG for the supply of biomass suspension.

Table A.1
Porosity and specific surface area—known values compared with image analysis results for a 'clean' filter bed

'Clean' filter quantities	Porosity, ϕ	Specific surface area, S (m^{-1})
Known value	0.950	5200
Image analysis result	0.995	17200

Appendix A. Image analysis method for determining void fraction and surface area of filter deposit

For a 'clean' filter bed (i.e. prior to filtration), the specific surface area S was also calculated from the known starting porosity ($\phi = 0.950$) and average fibre diameter ($d_f = 39$ μm by scanning electron microscopy) of the polyester fibre matrix, according to:

$$S = \frac{4\pi d_f V(1-\phi)}{V\pi d_f^2} = \frac{4(1-\phi)}{d_f} \tag{7}$$

where V is the section volume. For a void fraction of 0.95, $S = 5200\,m^{-1}$.

For the special case of a 'clean' filter medium, the values of ϕ and S are compared with the image analysis results in Table A.1. Notwithstanding the possibility that the local void fraction and specific surface area in the image section may be different to the average value, image analysis gives a clear over-prediction of both the porosity and the specific surface area. For the porosity, this is because the reflectance from fibres has a poor signal-to-noise ratio, and the analysis therefore incorrectly assigns some fibre voxels to be void voxels. The surface area calculation by image analysis gives the converse result in that the incorrect assignment of void voxels increases the number of fibre voxels with no nearest neighbour, thereby over-predicting the surface area. In addition, the limited resolution of the image stack gives the fibre surfaces an apparently 'rough' surface, enhancing the over-prediction of the values. For these reasons, the 'clean filter' porosity and surface areas obtained by the calculation in Eq. (7) were used in the further analysis.

Contrary to the reflectance signal from the polyester fibres, the fluorescence from biomass particles has a good signal-to-noise ratio throughout the image section. Since this signal is processed separately, it is possible to estimate the solid fraction and surface area contributions from the fluorescing biomass deposit and to add this to the known values for the fibres in the filter matrix.

References

[1] V. Antsiferov, S. Porozova, Foam ceramic filters for molten metals: reality and prospects, Powder Metall. Met. Ceram. 42 (9–10) (2003) 474–477.
[2] M. Becker, T. Georgian, H. Ambrose, J. Siniscalchi, K. Fredrick, Estimating flow and flux of ground water discharge using water temperature and velocity, J. Hydrol. 296 (1–4) (2004) 221–233.
[3] T.E. Bustnes, M.R. Mackley, The capture and release of biomass using a high voidage fibrous filter, Chem. Eng. Sci. 60 (19) (2005) 5206–5218.
[4] T.E. Bustnes, The removal of biomass from wastewater streams using a high voidage filter, Ph.D. Thesis, University of Cambridge, 2004.
[5] T.E. Bustnes, C.F. Kaminski, M.R. Mackley, Direct visualization of flowing biomass capture and release within a fibrous matrix, Biochem. Eng. J. 18 (3) (2004) 231–234.

[6] H.-W. Chiang, C. Tien, Dynamics of deep bed filtration. II. Experiment, AIChE J. 31 (8) (1985) 1360–1371.
[7] H. Cikurel, M. Rebhun, A. Amirtharajah, A. Adin, Wastewater effluent reuse by in-line flocculation filtration process, Water Sci. Technol. 33 (10–11) (1996) 203–211.
[8] L.S. Clesceri, A.E. Greenberg, A.D. Eaton, Standard Methods for the Examination of Water and Wastewater, 20th ed., APHA, AWWA, WEF, Washington, DC, 1998.
[9] J.L. Darby, D.F. Lawler, Ripening in depth filtration—effect of particle-size on removal and head loss, Environ. Sci. Technol. 24 (7) (1990) 1069–1079.
[10] G. Gesan-Guiziou, G. Daufin, E. Boyaval, Critical stability conditions in skimmed milk crossflow microfiltration: impact on operating modes, Lait 80 (1) (2000) 129–138.
[11] J. Gregory, The density of particle aggregates, Water Sci. Technol. 36 (4) (1997) 1–13.
[12] J. Herzig, D. Leclerc, P. LeGoff, Flow of suspensions through porous media—application to deep bed filtration, Ind. Eng. Chem. 62 (1970) 8.
[15] C.H. Ko, M. Elimelech, The "shadow effect" in colloid transport and deposition dynamics in granular porous media: measurements and mechanisms, Environ. Sci. Technol. 34 (17) (2000) 3681–3689.
[16] H. Ladva, P. Tardy, P. Howard, E. Dussan, Multiphase flow and drilling-fluid filtrate effects on the onset of production, SPE J. 6 (4) (2001) 425–432.
[17] X. Li, Y. Yuan, Settling velocities and permeabilities of microbial aggregates, Water Res. 36 (12) (2002) 3110–3120.
[18] Metcalf & Eddy, Wastewater Engineering: Treatment and Reuse, 4th ed., McGraw Hill, New York, 2003.
[19] J. Moghadasi, H. Muller-steinhagen, M. Jamialahmadi, A. Sharif, Theoretical and experimental study of particle movement and deposition in porous media during water injection, J. Pet. Sci. Eng. 43 (3–4) (2004) 163–181.
[20] D.C. Moran, M.C. Moran, R.S. Cushing, D.F. Lawler, Particle behavior in deep-bed filtration. Part 1. Ripening and breakthrough, J. Am. Water Works Assoc. 85 (12) (1993) 69–81.
[21] T. Mulder, R. Gimbel, Particle deposition in fiber balls—a basis to develop synthetic collectors for deep-bed filters, Colloids Surf. 39 (1–3) (1989) 207–226.
[22] M. Muller, R. Schneeberger, D. Wieckhusen, M. Cooper, Example of finishing technologies as key elements for successful active pharmaceutical ingredient process development, Org. Process Res. Dev. 8 (3) (2004) 376–380.
[23] H. Ngo, S. Vigneswaran, Application of floating medium filter in water and waste-water treatment with contact-flocculation filtration arrangement, Water Res. 29 (9) (1995) 2211–2213.
[25] S. Rege, H. Fogler, Network model for straining dominated particle entrapment in porous media, Chem. Eng. Sci. 42 (7) (1987) 1553–1564.
[26] E. Rodier, J. Dodds, D. Leclerc, G. Clément, Changes in fluid residence time distribution during deep-bed filtration, Chem. Eng. J. 68 (2–3) (1997) 131–138.
[27] J. Saiers, D. Genereux, C. Bolster, Influence of calibration methodology on ground water flow predictions, Ground Water 42 (1) (2004) 32–44.
[28] N. Schorghofer, B. Jensen, A. Kudrolli, D. Rothman, Spontaneous channelization in permeable ground: theory, experiment, and observation, J. Fluid Mech. 503 (2004) 357–374.
[29] L. Spielman, S.L. Goren, Model for predicting pressure drop and filtration efficiency in fibrous media, Environ. Sci. Technol. 2 (1968) 279–287.
[30] D. Tao, J. Groppo, B. Parekh, Enhanced ultrafine coal dewatering using flocculation filtration processes, Miner. Eng. 13 (2) (2000) 163–171.
[31] C. Tien, Hydrosol deposition in porous media: the effect of surface interactions, Adv. Powder Technol. 11 (1) (2000) 9–56.
[32] C. Tien, A.C. Payatakes, Advances in deep bed filtration, AIChE J. 25 (5) (1979) 737–759.
[33] H. Vaziri, Y. Xiao, R. Islam, A. Nouri, Numerical modeling of seepage-induced sand production in oil and gas reservoirs, J. Pet. Sci. Eng. 36 (1–2) (2002) 71–86.
[34] S. Vigneswaran, H. Ngo, K. Hashimoto, T. Hasegawa, Y. Watanabe, High rate floating medium flocculation-filtration with in-line polysilicato-iron (psi) addition, Environ. Technol. 21 (3) (2000) 317–325.
[35] R. Wakeman, D. Burgess, R. Stark, The Howden-Wakeman filter in wastewater treatment, Filtr. Sep. 31 (2) (1994) 183–187.
[36] R.M. Wu, G.W. Tsou, D.J. Lee, Estimate of sludge floc permeability, Chem. Eng. J. 80 (1–3) (2000) 37–42.
[37] Y. Yang, X. Zhang, Z. Wang, Oilfield produced water treatment with surface-modified fiber ball media filtration, Water Sci. Technol. 46 (11–12) (2002) 165–170.
[38] A. Zadeh, J. Campbell, Filter systems for high velocity liquid metal flow, Int. J. Cast. Met. Res. 17 (2) (2004) 99–106.